Biophysical Journal
Article

Biophysical Society

The Secreted Signaling Protein Wnt3 Is Associated with Membrane Domains In Vivo: A SPIM-FCS Study

Xue Wen Ng,[1,2] Cathleen Teh,[3] Vladimir Korzh,[3,4] and Thorsten Wohland[1,2,4,*]
[1]Department of Chemistry and [2]Center for BioImaging Sciences, National University of Singapore, Singapore, Singapore; [3]Institute of Molecular and Cell Biology, Agency for Science, Technology and Research, Singapore, Singapore; and [4]Department of Biological Sciences, National University of Singapore, Singapore, Singapore

ABSTRACT Wnt3 is a morphogen that activates the Wnt signaling pathway and regulates a multitude of biological processes ranging from cell proliferation and cell fate specification to differentiation over embryonic induction to neural patterning. Recent studies have shown that the palmitoylation of Wnt3 by Porcupine, a membrane-bound O-acyltransferase, plays a significant role in the intracellular membrane trafficking of Wnt3 and subsequently, its secretion in live zebrafish embryos, where chemical inhibition of Porcupine reduced the membrane-bound and secreted fractions of Wnt3 and eventually led to defective brain development. However, the membrane distribution of Wnt3 in cells remains not fully understood. Here, we determine the membrane organization of functionally active Wnt3-EGFP in cerebellar cells of live transgenic zebrafish embryos and the role of palmitoylation in its organization using single plane illumination microscopy-fluorescence correlation spectroscopy (SPIM-FCS), a multiplexed modality of FCS, which generates maps of molecular dynamics, concentration, and interaction of biomolecules. The FCS diffusion law was applied to SPIM-FCS data to study the subresolution membrane organization of Wnt3. We find that at the plasma membrane in vivo, Wnt3 is associated with cholesterol-dependent domains. This association reduces with increasing concentrations of Porcupine inhibitor (C59), confirming the importance of palmitoylation of Wnt3 for its association with cholesterol-dependent domains. Reduction of membrane cholesterol also results in a decrease of Wnt3 association with cholesterol-dependent domains in live zebrafish. This demonstrates for the first time, to our knowledge, in live vertebrate embryos that Wnt3 is associated with cholesterol-dependent domains.

INTRODUCTION

The development of a complex multicellular organism from a fertilized egg involves the concerted regulation of cell proliferation, migration, differentiation, and death in synchrony over a wide range of spatial and temporal scales. Wnt3, a signaling molecule that belongs to the Wnt family of cysteine-rich proto-oncogene signaling glycoproteins (Wnts), regulates such processes and is evolutionally conserved in metazoans. Its signaling plays key roles in numerous biological processes including, but not limited to, neural pattering and vertebrate primary axis formation (1–6), and regulation of neurogenesis by inhibiting granule cell progenitors that leads to the suppression of medulloblastoma formation (7). The impairment of Wnt3 signaling by a homozygous nonsense mutation in the human Wnt3 gene leads to a rare human genetic disorder known as Tetra-amelia, characterized by the failure to develop all four limbs and miscarriage (8).

There is increasing interest in the intracellular trafficking pathway of functional Wnts in Wnt-producing cells and in particular their localization on cell membranes, necessary for secretion (9,10). The membrane targeting ability of Wnts in Wnt-producing cells is imparted by a posttranslational lipid modification, known as palmitoylation, that Wnts undergo in the endoplasmic reticulum (ER), which confers hydrophobicity upon them. Palmitoylation of murine Wnt3a occurs at the cysteine residue (C77) with palmitic acid and at the serine residue (S209) with palmitoleic acid (11,12). These palmitoylation sites are highly conserved among all members of the Wnt family except *Drosophila* WntD, suggesting similar lipid modifications in Wnt proteins (11–13). Palmitoylation of proteins is vital for their membrane targeting, binding, and localization into plasma membrane domains and their respective functionalities (14–17). For Wnt proteins, palmitoylation is proposed to be regulated by Porcupine, a membrane-bound O-acyltransferase, in the ER (18–21).

Submitted February 4, 2016, and accepted for publication June 16, 2016.
*Correspondence: twohland@nus.edu.sg
Editor: Paul Wiseman.
http://dx.doi.org/10.1016/j.bpj.2016.06.021

Currently, there is limited information on the membrane domain association of palmitoylated Wnts. Most studies used biochemical experiments in vitro and ex vivo that are prone to artifacts and provide only indirect evidence of domain localization (12,22,23). Furthermore, in two-dimensional cell cultures, transiently transfected Wnts often remain in the ER and do not reach the plasma membrane (9,24). This was also observed by our group previously for Wnt3 (unpublished results). Therefore, it is important to study Wnt proteins, and in particular Wnt3, in a three-dimensional physiological environment that does not compromise Wnt3 distribution and function.

In this study, we used the *wnt3* promoter-driven zebrafish transgenic line, Tg(−4.0*wnt3*:Wnt3EGFP)^{F3}, previously generated by our group, which expresses functional Wnt3-EGFP in the brain, particularly the cerebellum. We already used these transgenics and a combination of confocal fluorescence correlation spectroscopy (FCS) and imaging techniques to study the effect of membrane trafficking and secretion of functionally active Wnt3 proteins on cerebellum development (25). Our previous results confirmed the membrane localization of Wnt3-EGFP and the presence of a secreted soluble Wnt3 fraction by confocal imaging and FCS in live zebrafish embryos (25). In this study, we extend the previous work by employing single plane illumination microscopy-fluorescence correlation spectroscopy (SPIM-FCS) to measure protein diffusion in live cells and live zebrafish embryos (26). SPIM-FCS is a multiplexed camera-based imaging FCS modality (26–30) that combines SPIM with fast array detectors such as an electron-multiplying charged coupled device (EMCCD) camera (29). SPIM-FCS allows simultaneous FCS measurements on thousands of adjacent observation volumes to provide spatial maps of the diffusion coefficient (D) of a sample.

However, the results of SPIM-FCS measurements are diffraction-limited, which prevents the study of subresolution membrane domains. We thus adapt, in this study, the FCS diffusion law (31) to SPIM-FCS (SPIM-FCS diffusion law). The FCS diffusion law utilizes the spatial dependence of the diffusion coefficient of the probe molecule obtained from diffraction-limited FCS measurements to investigate the type of nanoscopic membrane organization exhibited by the probe. By using observation areas of different size, one can obtain information on whether the molecule diffuses freely or is hindered by obstacles, e.g., domains that can trap a particle or meshworks that constitute diffusion barriers. The FCS diffusion law is easily incorporated into SPIM-FCS due to the ability to perform binning of pixels postacquisition to create multiple observation areas from a single FCS measurement. Similar postprocessing was done earlier for the applications of imaging total internal reflection-FCS (ITIR-FCS), another imaging FCS modality, in live cells (32). Along with the excellent penetration ability of light sheet illumination of SPIM (33) into thick samples, the combination of SPIM-FCS with the FCS diffusion law presents a useful tool to investigate the membrane organization of proteins in live organisms.

To the best of our knowledge, this is the first demonstration of the FCS diffusion law adapted to SPIM-FCS and applied to in vivo samples. Our results show that Wnt3-EGFP in cerebellar cells of live, three days postfertilized (dpf) zebrafish embryos are confined in cholesterol-dependent membrane domains. Inhibition of Porcupine, and thus reduction of palmitoylation of Wnt3, by the small molecule Wnt inhibitor C59 reduces the extent of Wnt3-EGFP domain confinement in a dose-dependent manner. This indicates the importance of Wnt3 palmitoylation for its association with cholesterol-dependent domains of the plasma membrane.

MATERIALS AND METHODS

Sample preparations for giant unilamellar vesicles (GUVs), live cells and live zebrafish, and confocal imaging and FCS descriptions are provided in the Supporting Material.

SPIM-FCS instrumentation and data acquisition

SPIM-FCS measurements were conducted on a home-built SPIM system, for which the instrumental description is given in Krieger et al. (28) and Singh et al. (29). The SPIM setup has two diode-pumped solid-state laser lines, 488 nm (OBIS 488 nm LX; Coherent, Santa Clara, CA) and 561 nm (LMX-561S-25-COL-PP; Oxxius, Lannion, France), as excitation light sources. The 488- and 561-nm laser lines are beam-expanded by factors of 3.33 and 3.75, respectively, with a set of achromatic lenses (488 nm: $f_1 = 45$ mm and $f_2 = 150$ mm; and 561 nm: $f_1 = 40$ mm and $f_2 = 150$ mm, Edmund Optics, Singapore). The 561-nm laser line is reflected by a dichroic beamsplitter (LM01-613-25; Semrock, Rochester, NY) and passes through another dichroic beamsplitter (LM01-503-25; Semrock) that reflects the 488-nm laser line and couples it to the 561-nm laser line. Both laser lines are then reflected by a gimbal mirror to another beam expansion unit ($f_1 = 100$ mm and $f_2 = 230$ mm, Edmund Optics) and passed through an achromatic cylindrical lens ($f = 75$ mm, Edmund Optics) mounted on a combination of linear and rotation stages (z-stage: MVT 40B-Z, rotation stage: DT 40-D25; all stages are from OWIS, Staufen, Germany) to generate their respective light sheets. Each light sheet then overilluminates the back-focal plane of a low numerical aperture illumination objective (SLMPLN 20×/0.25; Olympus, Singapore) and is focused to produce a thin light sheet with thickness of ~1.2 μm. The working distance of 21 mm of the illumination objective provides sufficient space to bring the light sheets to the focal plane of the detection objective (LUMPLFLN 60×/1.0W, working distance = 2.0 mm; Olympus) placed orthogonal to the illumination objective. The sample mounting unit includes a custom-built sample chamber and motorized linear x-, y-, and z-stages along with a rotation stage (XYZ-linear stages: 3 × 8MT184-13DC and rotation stage: 8MR174-1-20; Standa, Vilnius, Lithuania). The water-immersion, high-numerical aperture, detection objective is placed in a mounting hole on one side of the chamber and mounted on a piezo flexure objective scanner (P-721 PIFOC; Physik Instruments, Singapore) for controlling the objective with nanometer precision. The sample is placed in the sample chamber and excited with the respective laser light sheets (488 nm: GFP-glycosylphosphatidylinositol (GPI) anchored protein (AP), Wnt3-EGFP, and Lyn-EGFP; 561 nm: RhoPE and DiI-C_{18}) to emit fluorescence that is collected by the detection objective and passed through an objective tube lens (LU074700, $f = 180$ mm; Olympus). The fluorescence signal is then split into two channels by a dual imaging optics unit (DV2; Photometrics,

Tucson, AZ, and razor edge 568-nm notch filter; Thorlabs, Newton, NJ; BLP01-488R-25, FF03-525/50-25, and LP02-568RU-25; Semrock), which consists of a 568-nm notch filter and a 488-nm long-pass filter for rejection of scattered laser light and two emission filters to select for the green and red channels, respectively, for detection by an EMCCD camera (Andor iXon3 860, 128 × 128 pixels; Andor Technology, South Windsor, CT). The pixel size in the object plane is 0.4 μm before 60× magnification from 24 μm of pixel size in the image plane and each channel consists of 64 × 128 pixels.

For data acquisition in SPIM-FCS, a stack of 50,000 images with variable regions of interest, depending on the sample under study, were taken by the software Andor Solis for Imaging (ver. 4.18.30004.0; Andor Technology) of the EMCCD camera at frame rates of 500 (for GFP-GPI AP, Wnt3-EGFP, and Lyn-EGFP) and 1000 (for RhoPE and DiI-C_{18}) frames per second. The background is accounted for by taking the lowest count value in a given file. The stack of images was then saved as a 16-bit Tiff file and data analysis was conducted by loading the image stack in Imaging_FCS 1.45, a home-written plugin in the software ImageJ (U. S. National Institutes of Health, Bethesda, MD; available at: http://staff.science.nus.edu.sg/~chmwt/imfcs_image_j_plugin.html). The fluorescence fluctuations of each pixel were fitted with the SPIM-FCS fitting model:

$$G_{\mathrm{SPIM}}(\tau)=\frac{1}{N}\cdot\left\{\frac{\sqrt{4D\tau+\omega_{xy}^2}}{\sqrt{\pi}\cdot a}\times\left[e^{\left(-\frac{a^2}{4D\tau+\omega_{xy}^2}\right)}-1\right]+\mathrm{erf}\left(\frac{a}{\sqrt{4D\tau+\omega_{xy}^2}}\right)\right\}^2\times\left(1+\frac{4D\tau}{\omega_Z^2}\right)^{-\frac{1}{2}}+G_\infty. \tag{1}$$

Equation 1 describes the theoretical model of the autocorrelation function (ACF) $G(\tau)$ as a function of lag time (τ) for a three-dimensional diffusion process provided by the SPIM illumination scheme and EMCCD detection (28,29,34). The character a is the camera pixel side length in the object plane, ω_{xy} and ω_z are the $1/e^2$ radii of the point spread function in the lateral and axial direction respectively of the maximum intensity (I_0) at the focus of the observation volume, D is the diffusion coefficient of the particle, $\langle C\rangle$ is the average concentration and G_∞ is the convergence value of the ACF at infinity lag times. The camera pixel size a at the object plane is 400 nm. The value ω_{xy} was calibrated with 100-nm fluorescent microspheres in 1 × PBS by the method described by our group previously (28,29,35). The value ω_z was approximated from the measured light sheet width fitted with a Gaussian function of $1/e^2$ radii and calibrated before every experiment. The fitting parameters are the number of particles (N), diffusion coefficient (D), and the convergence value (G_∞). For membrane measurements, ω_z was set at a large value, close to infinity, in Eq. 1 to fit for lateral membrane diffusion of membrane probes. Maps of the diffusion coefficient (D) and the number of particles (N) are then obtained. The goodness of fit is determined by the χ^2-value of the fit.

FCS diffusion law for SPIM

The theory of the FCS diffusion law and its various implementation are given here (31,36,37). Briefly, the FCS diffusion law utilizes the spatial dependence of the diffusion coefficient of membrane probes to gain access to various membrane organizational features. The FCS diffusion law analysis plots the diffusion time (τ_D) of a probe against the observation area (A_{eff}). In the case of free diffusion, the FCS diffusion law plot is linear. On the other hand, both hindered diffusion with domain confinement and hop diffusion due to meshwork compartmentalization exhibit specific transitions that lead to nonlinearity in the FCS diffusion law plots. However, because the diffraction-limited observation areas created by most optical setups are larger than either the domains or mesh sizes expected in the biological samples, such nonlinear transitions cannot be observed directly. To resolve this limitation, one can extrapolate the experimental FCS diffusion law plots to zero observation area to obtain the y-intercept value (τ_0), which is positive for hindered diffusion with domain confinement, negative for hop diffusion due to meshwork compartmentalization, and zero for free diffusion. The stronger the domain confinement, the larger is the positive τ_0 value. Domain density, domain size, and partitioning probability into domains are increasing functions of the positive τ_0 values for domain confinement. On the other hand, the absolute magnitude of the negative τ_0 value for meshwork compartmentalization is influenced by mesh size, density, and hop frequency of the probe.

The abovementioned dependence of diffusion time with area can be empirically integrated into the following SPIM-FCS diffusion law equation:

$$\tau_D\left(A_{\mathrm{eff}}\right)=\tau_0+\frac{A_{\mathrm{eff}}}{D_{\mathrm{eff}}}, \tag{2}$$

where D_{eff} is the effective diffusion coefficient defined as the inverse of the slope of the FCS diffusion law plot and τ_0 is the so-called FCS diffusion law intercept that takes zero, positive, and negative values depending on the diffusion modes. Various observation areas are created by pixel-binning postacquisition because different bin sizes in imaging FCS can be accurately determined by convoluting the detection area (a) of a given bin size (e.g., 1×1, 2×2, 3×3, etc.) with the ω_{xy} of the SPIM optical system (34,35). The SPIM-FCS diffusion law analysis was also performed in the Imaging_FCS 1.45 ImageJ plugin mentioned earlier.

RESULTS AND DISCUSSION

SPIM-FCS provides two important advantages in imaging FCS. First, it allows us to create three-dimensional diffusion coefficient maps by scanning the light sheet through the sample and provide a z-stack of diffusion maps. Proof-of-principle experiments on GUVs and cells are given in the Figs. S1 and S2 and Table S1 in the Supporting Material. They demonstrate that, due to the asymmetry of the SPIM-FCS observation volume, the measured diffusion coefficients need in general to be corrected for geometrical effects (Fig. S3). However, for angles of the membrane in respect to the light sheet of $<40^\circ$ the bias in D is well within the SD of the measurement. This curvature effect is more pronounced in GUVs, shown by a progressive decrease of D with increasing curvature (from $z = 0$ μm to $z = 6.0$ μm; Table S1); however, it is negligible for cells, with no z-dependence of D (Table S1), due to the more flattened geometry of cells compared to GUVs. One should note, however, that if there are strong undulations in terms of membrane ripples, the diffusion coefficient would change irrespective of the overall membrane inclination (38,39). Second, SPIM-FCS allows applying the FCS diffusion law to probe the nanoscopic organization of the sample. For the FCS diffusion law, though, the measurements have to be taken simultaneously on multiple contiguous pixels, which is not the case in a sequentially acquired z-stack. Therefore, to avoid any geometrical artifacts and to be able to apply the FCS diffusion law, all measurements in live cells and zebrafish were conducted by aligning the

membrane of interest parallel to the light sheet by rotating the sample (Fig. 1 *A*).

SPIM-FCS investigates membrane diffusion and organization of probes in live SH-SY5Y cells

We tested the feasibility of the SPIM-FCS diffusion law by determining the diffusion coefficients and membrane organization of commonly used membrane probes. For this purpose, DiI-C_{18} was used as a marker for free diffusion and GFP-GPI AP as a cholesterol-dependent domain marker in SH-SY5Y cell membranes (40,41). In this context, it is worth noting that plasma membrane domains can be broadly classified into two categories: (1) cholesterol-dependent domains including lipid rafts (enriched with sphingolipids and cholesterol) and caveolae domains (mainly contains glycosphingolipids and cholesterol), which are disturbed by membrane cholesterol removal; and (2) cholesterol-independent domains that remain undisturbed upon membrane cholesterol removal (42,43). These domains are suggested to influence and regulate cellular processes such as membrane trafficking, endocytosis, signal transduction, and host–pathogen interactions (42–47). Live-cell SPIM-FCS measurements were conducted by placing the upper membrane of the cell at the focal plane of the detection objective, aligned to the thinnest portion of the light sheet (Fig. 1 *A*) (27). As mentioned earlier, we orient the upper membrane of cells parallel to the light sheet, to avoid artifacts due to the nonisotropic observation volume (see the Supporting Material). This provides larger areas for measurements (Fig. S3 and Table S1), as required for FCS diffusion law analysis because a homogenous membrane coverage is needed for binning of pixels to generate points on the FCS diffusion law plot at various binned areas. This cannot be achieved at z-positions below the upper membrane, which consists of only the membrane boundary, resulting in insufficient membrane area for FCS diffusion law analysis. The coverslip is tilted at ~5° to prevent reflection and scattering of the light sheet it generates.

The D of DiI-C_{18} and GFP-GPI AP labeled live SH-SY5Y cell membranes were 2.24 ± 0.67 $\mu m^2/s$ and 0.35 ± 0.15 $\mu m^2/s$, respectively (Table 1), which agrees well with previous measurements at the lower plasma membrane of the same cell line by ITIR-FCS (48). The representative ACFs and corresponding fits for both probes for a representative cell are depicted in Fig. 1, *B* and *C*, respectively. The representative D maps of both membrane probes are also portrayed in the insets of Fig. 1, *B* and *C*, to show heterogeneous diffusion of both probes and their vast difference on the cell membrane. The D values indicated in Fig. 1, *B*

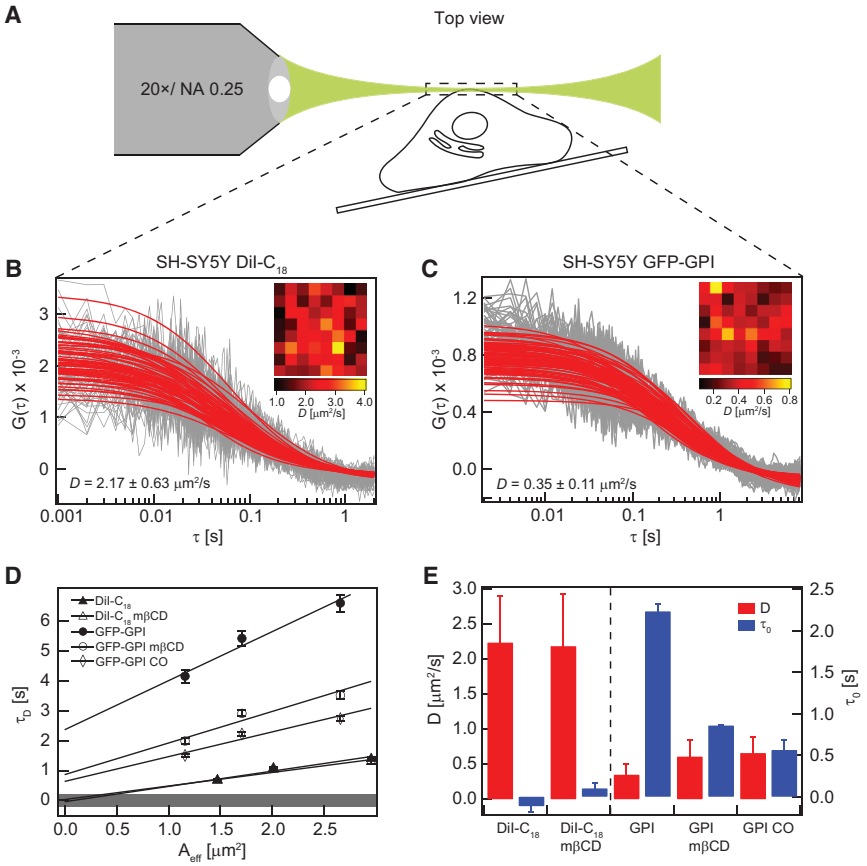

FIGURE 1 SPIM-FCS and SPIM-FCS diffusion law measurements on the upper membranes of live SH-SY5Y cells and the effect of cholesterol extraction on the membrane localization of DiI-C_{18} and GFP-GPI AP on live SH-SY5Y cell membranes. (*A*) Schematic of SPIM-FCS measurement on a live cell. Representative ACFs of (*B*) DiI-C_{18} (non-raft marker) labeled SH-SY5Y cell and (*C*) GFP-GPI AP (raft marker) transfected SH-SY5Y cell. In the inset, the D maps are shown. (*D*) Representative SPIM-FCS diffusion law plots of the plasma membranes of DiI-C_{18} labeled cells and GFP-GPI AP transfected cells before and after 2.5 mM mβCD treatment (30 min) and 1 U/mL COase treatment (30 min) for GFP-GPI AP transfected cells only. The grey shaded area represents the range of the limit of the SPIM-FCS diffusion law intercept (τ_0) for free diffusion. (*E*) D and τ_0 values for DiI-C_{18} (3 cells with 337 ACFs collected), GFP-GPI AP (5 cells with 446 ACFs collected), 2.5 mM mβCD-treated DiI-C_{18} (4 cells with 362 ACFs collected), 2.5 mM mβCD-treated GFP-GPI AP (2 cells with 164 ACFs collected), and 1 U/mL COase-treated GFP-GPI AP labeled SH-SY5Y cells (6 cells with 263 ACFs collected). To see this figure in color, go online.

TABLE 1 SPIM-FCS and SPIM-FCS Diffusion Law Results of Various Probes in Live SH-SY5Y Cells and Live Zebrafish Embryos

Sample	D [$\mu m^2/s$]	τ_0 [s]	$N_{cells/fish}$	$N_{measurement}$	N_{ACFs}
SH-SY5Y cells					
DiI-C_{18}	2.24 ± 0.67	−0.11 ± 0.07	3	5	337
DiI-C_{18} 2.5 mM mβCD	2.19 ± 0.75	0.10 ± 0.06	4	4	362
GFP-GPI AP	0.35 ± 0.15	2.24 ± 0.09	5	5	446
GFP-GPI AP 2.5 mM mβCD	0.61 ± 0.24	0.86 ± 0.01	2	2	164
GFP-GPI AP 1 U/mL COase	0.66 ± 0.23	0.56 ± 0.12	6	6	263
Zebrafish					
Wnt3-EGFP	0.98 ± 0.38	0.88 ± 0.13	3	4	164
Wnt3-EGFP 1% DMSO	1.01 ± 0.43	0.91 ± 0.18	3	5	180
Wnt3-EGFP 2.5 μM C59	1.21 ± 0.54	0.67 ± 0.06	2	4	144
Wnt3-EGFP 5.0 μM C59	1.53 ± 0.68	0.36 ± 0.08	1	4	144
Wnt3-EGFP 7.5 μM C59	1.96 ± 0.77	0.31 ± 0.03	3	4	144
Wnt3-EGFP 2.5 mM mβCD	2.02 ± 1.07	0.34 ± 0.03	2	5	180
Wnt3-EGFP 1 U/mL COase	1.51 ± 0.71	0.40 ± 0.09	3	5	180
Lyn-EGFP	0.97 ± 0.58	0.81 ± 0.33	2	3	121
Lyn-EGFP 5.0 μM C59	0.94 ± 0.44	0.83 ± 0.10	2	3	108
Lyn-EGFP 2.5 mM mβCD	1.82 ± 0.83	0.27 ± 0.03	2	4	144

Data are represented as mean ± SD of number of ACFs for D and mean ± SD of number of measurements for τ_0.

and C, are obtained from the representative D maps. For similar experiments on other cell lines, refer to Bag et al. (32,48). These D values are calculated after averaging over multiple measurements (337 ACFs for DiI-C_{18} from three cells and 446 ACFs for GFP-GPI AP from five cells). D values of GFP-GPI AP for individual measurements can be found in Fig. S4 *A*. The ratio of D of DiI-C_{18} and GFP-GPI AP is 6.4 (Table 1), which is close to the factor of ~5 observed for HeLa cells at 298 K measured by ITIR-FCS (48). This is consistent with their respective localization, as DiI-C_{18} resides mainly in the fluid matrix of unsaturated phospholipids in the membrane, which exhibits free diffusion with negligible confinement. In contrast, GFP-GPI AP localizes primarily in cholesterol-dependent domains, which impedes its mobility and leads to confinement as these domains are more ordered and tightly packed than the surrounding fluid lipid matrix of unsaturated phospholipids (41).

SPIM-FCS diffusion law analysis was performed on DiI-C_{18}- and GFP-GPI AP-labeled live SH-SY5Y cell membranes to investigate their diffusion modes. The areas of the upper membrane where SPIM-FCS measurements were conducted to generate the D maps for both DiI-C_{18} and GFP-GPI AP-labeled SH-SY5Y cells were also used to deduce the type of membrane organization each probe exhibits by the FCS diffusion law analysis. Because the precision of the FCS diffusion law is affected by pixel size in the object plane of the optical system (34), it is important to determine the margin of error of the FCS diffusion law intercept (τ_0) for free diffusion in SPIM-FCS diffusion law. This was found to vary between ± 0.2 s from measurements at the upper membrane of RhoPE-labeled freely diffusing DOPC/DOPG (10:1) GUVs (Fig. S5 *A*). Processes with τ_0 values found within this range are indistinguishable from free diffusion by SPIM-FCS diffusion law. This is shown as a shaded area in all the SPIM-FCS diffusion law plots (Fig. 1 *D*; and see Figs. 3 *A* and 4 *A*). For SH-SY5Y cells, the intercept of the FCS diffusion law plot of DiI-C_{18} was −0.11 ± 0.07 s, well within ± 0.2 s and thus indicating free diffusion, while GFP-GPI AP shows domain confinement with τ_0 of 2.24 ± 0.09 s (Fig. 1, *D* and *E*; Table 1). Measurements were performed on 3–5 cells and the individual τ_0 values of GFP-GPI AP were consistent for multiple cells (Fig. S4 *A*). This is in agreement with the large factor of difference of 6.4 in their diffusion coefficients, which presumably is a result of fast and free diffusion of DiI-C_{18} in the fluid phospholipid region of the plasma membrane and confined diffusion of GFP-GPI AP localized in more viscous and ordered cholesterol-dependent domains. The SPIM-FCS diffusion law intercepts that were obtained for model and live-cell membranes are consistent with previous ITIR-FCS measurements (Fig. S5 and Table S2).

Next, we tested the sensitivity of the SPIM-FCS diffusion law to detect changes in membrane organization. GFP-GPI AP-labeled cells were incubated with 2.5 mM methyl-β-cyclodextrin (mβCD), a reagent that depletes membrane cholesterol, and were measured before treatment and 30 min after. The concentration of 2.5 mM mβCD used in this study does not affect the viability of cells (49). Our results show that after mβCD treatment, domain confinement of GFP-GPI AP decreased, where its τ_0 value decreased to 0.86 ± 0.01 s (decrease by 61.6%) with a concomitant increase in its D value to 0.61 ± 0.24 $\mu m^2/s$ (increase by 74.3%) (Fig. 1, *D* and *E*; Table 1). This suggests that GFP-GPI AP is confined to cholesterol-dependent domains, which is consistent with previous ITIR-FCS measurements made on the lower membrane of GFP-GPI AP-transfected CHO-K1 cells (32). Interestingly, the confinement of GFP-GPI AP was not completely removed even after 30 min of mβCD treatment. This could be due to either incomplete cholesterol removal as a result of mβCD saturation (32) or the recruitment of more lipids to the plasma membrane by

the cell as a response to perturbation caused by a drug, which may cause some recovery of the membrane properties (50). The SPIM-FCS results are similar to measurements by ITIR-FCS on the same biological system, showing the applicability of the SPIM-FCS diffusion law to determine mobility and membrane organization of molecules of interest. However, cholesterol removal leads to a somewhat smaller decrease of τ_0 on the upper cell membrane of SH-SY5Y cells compared to the lower membrane measured in CHO-K1 cells by ITIR-FCS in our earlier work (32), where GFP-GPI AP reverted to free diffusion, i.e., $\tau_0 < 0.2$ s after mβCD treatment. This could be due to a difference between cell lines or membranes (attached membrane mimics basolateral membrane in living tissue versus unattached membrane, which mimics apical membrane in living tissue). This problem has to be addressed in the future. Nevertheless, GFP-GPI AP showed a consistent strong decrease of τ_0 (~60%) in all measurements. As a control, DiI-C_{18}-labeled SH-SY5Y cells were also treated with 2.5 mM mβCD for 30 min and measured. Both D (2.24 $\pm$ 0.67 $\mu m^2/s$ to 2.19 $\pm$ 0.75 $\mu m^2/s$) and τ_0 (-0.11 ± 0.07 s to 0.10 ± 0.06 s; these parameters indicate free diffusion) values of DiI-C_{18} remain almost unchanged before and after cholesterol removal (Fig. 1, D and E; Table 1). This indicates that mβCD treatment does not affect the membrane dynamics and organization of freely diffusing DiI-C_{18} in the fluid matrix of unsaturated phospholipids in the membrane and that the reduction in domain confinement and increased membrane diffusion of GFP-GPI AP after cholesterol removal by mβCD likely originates from the disruption of cholesterol-dependent domains of the plasma membrane, where GFP-GPI AP localizes.

Because it was reported that mβCD removes cholesterol preferentially from the liquid-disordered phase in phase-separated GUVs (51), we treated GFP-GPI AP-transfected SH-SY5Y cells with 1 U/mL cholesterol oxidase (COase), which reduces cholesterol content with no phase preference by catalyzing the oxidation of cholesterol to cholestenone as a secondary drug treatment method for the investigation of cholesterol-dependent domain confinement of GFP-GPI AP. SH-SY5Y cells transfected with GFP-GPI AP were treated with 1 U/mL COase for 30 min at 37°C in 5% (v/v) CO_2 humidified environment and measured thereafter. Similar to 2.5 mM mβCD treatment, domain confinement of GFP-GPI AP decreased upon 1 U/mL COase treatment, where τ_0 decreased by 75% (2.24 $\pm$ 0.09 s to 0.56 $\pm$ 0.12 s), and GFP-GPI AP became more freely diffusing with an increase of 88.6% in D (0.35 $\pm$ 0.15 $\mu m^2/s$ to 0.66 $\pm$ 0.23 $\mu m^2/s$) (Fig. 1, D and E; Table 1). Lenne et al. (52) observed similar outcomes for GFP-GPI AP-transfected COS-7 cells where GFP-GPI AP's confinement was abolished after 1 U/mL COase treatment (30 min). Residual domain confinement of GFP-GPI AP in SH-SY5Y cells was also observed in this experiment, after 30 min of 1 U/mL COase treatment as opposed to a previous report (52). This is likely due to reasons explained earlier for the incomplete removal of domain confinement of GFP-GPI AP by mβCD treatment. Therefore, cholesterol depletion by both 2.5 mM mβCD and 1 U/mL COase treatment reorganizes the plasma membrane and reduces the domain confinement of GFP-GPI AP probably by disrupting cholesterol-dependent domains. This is consistent with STED-FCS diffusion law measurements where both mβCD and COase treatments reduced the trapping time of GPI-anchored protein in Ptk2 cells (53).

Comparative analysis of Wnt3-EGFP diffusion by confocal FCS and SPIM-FCS

The dynamics of both membrane-bound and fast-diffusing Wnt3-EGFP in live transgenic zebrafish embryos were reported earlier by our group based on confocal FCS measurements (25). The confocal FCS data on membrane was fitted with a two-component model with triplet state contribution to yield the diffusion coefficients and fractions of two diffusive species: (1) a fast component, which corresponds to that of fast-diffusing Wnt3 in the intracellular and extracellular space (D ~30 $\mu m^2/s$, Fraction ~40%); and (2) a slow-moving component, which represents the membrane-bound Wnt3-EGFP (D ~1 $\mu m^2/s$, Fraction ~60%). Although confocal FCS provides information on Wnt3-EGFP diffusion in live zebrafish, it can only measure one point at a given time, which limits the statistical reliability of data collected. Using Wnt3-EGFP in live zebrafish as an example, the number of ACFs collected per cerebellar cell of the zebrafish embryo for a single SPIM-FCS measurement is 36 at the apical membrane with a measurement time of 100 s. On the other hand, the number of ACFs collected in a given cerebellar cell for sequential confocal FCS measurements is typically 9 (3 points $\times$ 3 measurements per point) with a measurement time of 30 s for each measurement (total measurement time of 270 s). Thus SPIM-FCS outperforms confocal FCS in terms of its greater statistics of data generated in a much shorter measurement time compared to confocal FCS for the same number of measurement points. Because a single multiplexed SPIM-FCS measurement contains multiple well-defined observation areas required for the FCS diffusion law analysis, one can directly determine the membrane organization of the probe molecule from the same raw data. It is possible to obtain the FCS diffusion law plot with confocal FCS by conducting multiple confocal FCS measurements at different spot sizes. However, it is technically demanding to create spots of different sizes in the confocal system as it requires modification of the original confocal instrument by including a diaphragm or motorized variable beam expander (31,54). Furthermore, conducting multiple measurements at the same position in the live zebrafish is challenging, when we consider sample movement and drift, which becomes more significant with longer measurement times.

We first applied SPIM-FCS to study the diffusion properties of Wnt3-EGFP on cell membranes of the cerebellum and subsequently performed SPIM-FCS diffusion law analysis on the same set of data to investigate its membrane organization in live zebrafish. Three dpf-old Wnt3-EGFP-expressing zebrafish embryos were anesthetized with 0.05% (w/v) tricaine solution for 30 min and mounted into a capillary tube with 1% low melting point agarose. Measurements were then conducted at the upper (apical) membrane of cerebellar cells expressing Wnt3-EGFP as illustrated in the bright-field and SPIM fluorescence images in Fig. 2 *A*. The focusing of the upper membrane was conducted similar to that described earlier for cells in culture. The membrane localization of Wnt3 in the cerebellar cells of live zebrafish embryos with and without C59 treatment (7.5 μM) was validated by imaging and confocal FCS measurements on deyolked Wnt3-EGFP transgenics in Fig. S6. The slow component in the confocal FCS measurements that reflects the membrane diffusion of Wnt3 is consistent with that of SPIM-FCS measurements for both untreated (Confocal FCS: 0.83 $\pm$ 0.28 $\mu m^2/s$, SPIM-FCS: 0.98 $\pm$ 0.38 $\mu m^2/s$) and 7.5 μM C59-treated embryos (Confocal FCS: 1.60 $\pm$ 0.30 $\mu m^2/s$, SPIM-FCS: 1.96 $\pm$ 0.77 $\mu m^2/s$) (Fig. S6 *D*; Table 1). The fast diffusion component in the confocal FCS results, corresponding to the soluble fraction of Wnt3, is too fast to be captured by the slow frame rate of SPIM-FCS (500 Hz) (Fig. S6 *D*). The *D* of Wnt3-EGFP in the zebrafish embryos was 0.98 $\pm$ 0.38 $\mu m^2/s$ (Table 1; and the representative ACFs from a single cell are shown in Fig. 2 *B*). *D* values of Wnt3-EGFP for individual measurements can be found in Fig. S4 *B*. The *D* of Wnt3-EGFP in live zebrafish from SPIM-FCS measurements is comparable to that of the membrane-bound fraction (~1 $\mu m^2/s$) of Wnt3-EGFP measured by confocal FCS but is far off the *D* of the fast-diffusing cytosolic and secreted Wnt3-EGFP fraction (~30 $\mu m^2/s$) from confocal FCS measurements (25). The low time resolution of SPIM-FCS used in this study (~1 ms) compared to confocal FCS (<1 μs) limits the measurement of the fast diffusing component (34). Although in some cases (~16% of all pixels) a two-component model with a fast diffusing coefficient on the order of 20 $\mu m^2/s$ seems to provide acceptable fits, we in fact verified by Bayes model selection on the SPIM-FCS data that the one-component model is always preferred over the two-component model for the SPIM-FCS data (55–58).

The palmitoylation of Wnt proteins is driven by Porcupine in the ER for its membrane targeting (18–21). This is further supported by the binding of Porcupine to the N-terminal 24-amino-acid domain of *Drosophila* Wingless at residues 83–106 (19), which contains the acylation site at cysteine residue (C93) (9). Furthermore, Takada et al. (12) determined that stable reduction in expression levels of Porcupine by siRNA treatment in L cell (mouse fibroblast) transfectants led to the reduction of Wnt3a acylation. Porcupine was also found to influence Wnt secretion, intracellular trafficking, and signaling (13,22,59–61). Therefore, we treated Wnt3-EGFP transgenic zebrafish embryos with 5 μM of Porcupine inhibitor C59 to determine the effect of palmitoylation on the membrane diffusion of Wnt3. Treatment with C59 led to a ~56% increase in *D* of

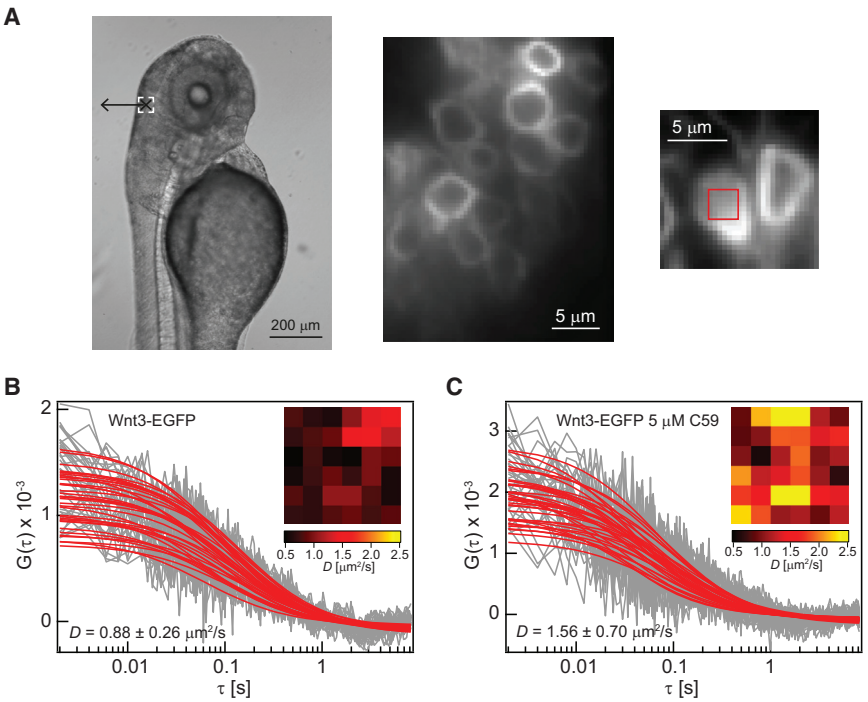

FIGURE 2 SPIM-FCS measurements on the apical membrane of cerebellar cells of live Wnt3-EGFP transgenic zebrafish. (*A*) Bright-field image of a 3-dpf zebrafish embryo. The dashed white box indicates the location of the cerebellum. The cross (×) and the left arrow (←) in the dashed white box indicate the directions of the light sheet illumination and detection, respectively. SPIM images of the cerebellar cells expressing Wnt3-EGFP in live transgenic zebrafish. The box on the rightmost image indicates a typical region of interest, where SPIM-FCS measurements were conducted. Representative ACFs of (*B*) a cerebellar cell expressing Wnt3-EGFP and (*C*) a cerebellar cell expressing Wnt3-EGFP after treatment with 5 μM C59. (*Insets*) Diffusion coefficient, *D*, maps. To see this figure in color, go online.

Wnt3-EGFP to 1.53 ± 0.68 $\mu m^2/s$ (Table 1; and the representative ACFs from a single cell are shown in Fig. 2 *C*). The overall increase in the membrane diffusion of Wnt3-EGFP was also reflected in the spatial distribution of *D* from the *D* maps before and after treatment with C59 (Fig. 2, *B* and *C*, *insets*). This increase in *D* was also reported in previous confocal FCS measurements (from 1 to 2.7 $\mu m^2/s$) (25). However, the *D* measured by confocal FCS increased by a factor of ~2.7 while the *D* measured by SPIM-FCS only increased by a factor of ~1.5. This discrepancy could be due to the different expression levels of Wnt3-EGFP of the different zebrafish transgenic lines used for confocal FCS and SPIM-FCS. The Tg(−4.0*wnt3*:Wnt3EGFP)^{F2} zebrafish transgenic line was used for the confocal FCS measurements while the Tg(−4.0*wnt3*:Wnt3EGFP)^{F3} line was used in SPIM-FCS measurements in this study. The Tg(−4.0*wnt3*:Wnt3EGFP)^{F3} line has a higher level of Wnt3-EGFP expression than the Tg(−4.0*wnt3*:Wnt3EGFP)^{F2}, which is required for SPIM-FCS measurements to achieve a sufficient signal/noise ratio. Therefore, with the same concentration of 5 μM C59 used to treat both transgenic lines, it is likely that the higher Wnt3 expression of Tg(−4.0*wnt3*:Wnt3EGFP)^{F3} compensates for the palmitoylation inhibition of Wnt3 as compared to Tg(−4.0*wnt3*:Wnt3EGFP)^{F2}, which led to a smaller increase in *D* of Wnt3 for Tg(−4.0*wnt3*:Wnt3EGFP)^{F3} in SPIM-FCS measurements than Tg(−4.0*wnt3*:Wnt3EGFP)^{F2} in the confocal FCS results. This is further supported by confocal FCS measurements conducted on deyolked embryos of the same Tg(−4.0*wnt3*:Wnt3EGFP)^{F3} line as that used for SPIM-FCS, where the *D* increased by similar factors of 1.8 (Confocal FCS) and 2 (SPIM-FCS) after treatment with 7.5 μM C59 (Fig. S6 *D*; Table 1). Nevertheless, this increase in *D* is indicative of the reduced confinement of Wnt3-EGFP on the plasma membrane upon the inhibition of palmitoylation of Wnt3 by C59.

C59 dose-dependence of Wnt3-EGFP membrane confinement in live zebrafish

We applied the SPIM-FCS diffusion law to the diffraction-limited in vivo SPIM-FCS data to study the nanoscopic membrane organization of Wnt3-EGFP in the cerebellum of live zebrafish. As mentioned earlier, one of the main advantages of SPIM-FCS is the possibility to generate variable observation areas from a single measurement to carry out FCS diffusion law analysis in vivo. Firstly, Wnt3-EGFP was confined to the plasma membrane domains with a positive τ_0 value of 0.88 ± 0.13 s (Fig. 3, *A* and *B*; Table 1). The τ_0 values of Wnt3-EGFP for three measurements can be found in Fig. S4 *B*. These domains cannot be detected by SPIM imaging as their size is below the diffraction-limit (Fig. 2 *A*, *rightmost image*). C59 was shown to influence the mobility (Fig. 2, *B* and *C*) and secretion of Wnt3-EGFP (25). Thus we performed SPIM-FCS diffusion law analysis on Wnt3-EGFP-expressing live zebrafish at various C59 concentrations. The decrease of τ_0 and concomitant increase of *D* with increasing C59 dosage demonstrates that membrane-bound Wnt3-EGFP is less confined in membrane domains (Fig. 3, *A* and *B*; Table 1). These results further support the previous study, where diffusion coefficient and membrane fraction of Wnt3-EGFP on cerebellar cells increased and decreased, respectively, with increasing C59 dosage (25). The reduction of membrane confinement of Wnt3-EGFP with C59 treatment could be due to several

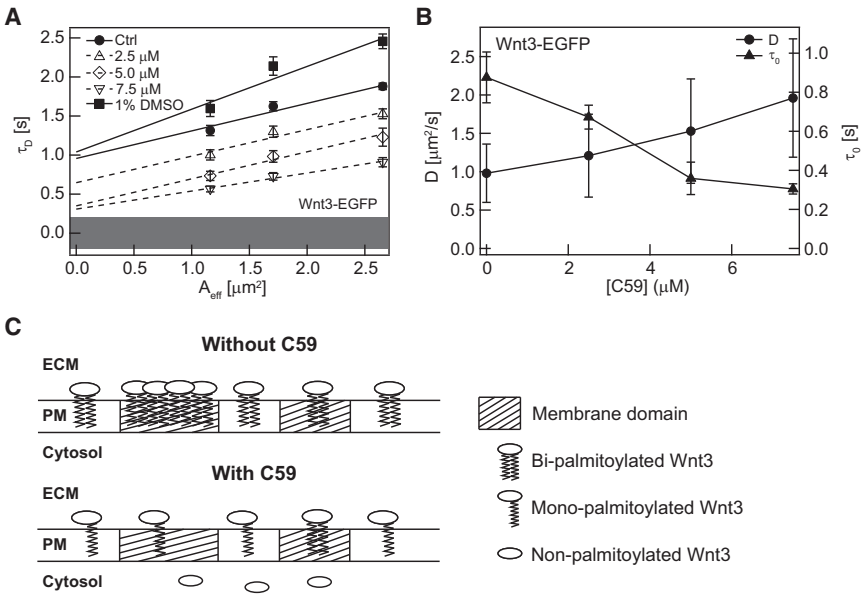

FIGURE 3 C59 concentration dependence of Wnt3-EGFP membrane domain association in cerebellar cells of live zebrafish. (*A*) Representative SPIM-FCS diffusion law plots of Wnt3-EGFP at different concentrations of the porcupine inhibitor C59. (*B*) *D* and τ_0 trends for Wnt3-EGFP at increasing dosage of C59. (*C*) Schematics of the possible membrane reorganization of Wnt3 before and after inhibition of Porcupine by C59. ECM, extracellular matrix; PM, plasma membrane.

reasons. Firstly, the inhibition of Porcupine by C59 could have reduced the amount of Wnt3 transported to the plasma membrane from the ER and led to a decrease of the membrane-bound Wnt3 and thus reducing its domain confinement (τ_0) (13,62). This is substantiated by the previous confocal FCS results, where the membrane-bound fraction of Wnt3 decreased with C59 concentration (25). The increasing of D of Wnt3 that correlates with increase of C59 concentration suggests a possible change in the palmitoylation states of Wnt3 from bipalmitoylated Wnt3 (both cysteine and serine sites) to monopalmitoylated Wnt3 and an overall alteration of its membrane organization upon Porcupine inhibition. Moreover, Porcupine catalyzes the palmitoylation of the serine residue, but not the cysteine residue of Wnt1 and Wnt3a proteins, further supporting the change in palmitoylation state of Wnt3 after C59 treatment (63,64). Monopalmitoylated Wnt3 proteins are likely to partition less into membrane domains than bipalmitoylated Wnt3 and localize mainly in the fluid phospholipid matrix of the membrane (Fig. 3 *C*, *schematics*), leading to an overall faster diffusion and decreased domain confinement of Wnt3 with increasing C59 concentration. In any scenario, the lipid modification of Wnt3 by Porcupine must be crucial for the membrane domain localization of Wnt3. As has been shown for other peripheral membrane proteins, palmitoylation can be a decisive factor in lipid raft localization (14–17). The C59 dose-dependent response of Wnt3-EGFP diffusion and domain confinement indicates that Porcupine may not be completely inhibited at lower concentrations of C59 and a certain degree of palmitoylation activity remains. The highest concentration of C59 that we could administer for accurate quantification of Wnt3-EGFP dynamics and domain confinement was 7.5 μM. Further increase of C59 concentration leads to inhibitor precipitation in solution. In addition, high dose of C59 severely disturbs cerebellum development and affects its morphology. This poses a great challenge in conducting and comparing SPIM-FCS measurements in the same brain area. For instance, at concentrations of C59 above 50 μM administered to 36 h postfertilized (hpf) zebrafish larvae, cerebellum was distorted to an extent that prevented measurements of Wnt3-EGFP diffusion by SPIM-FCS. Note that administering concentrations of C59 above 5 μM to young (10 hpf) embryos caused the same effect. To ensure that τ_0 and D responses of Wnt3-EGFP are specific to Porcupine inhibition by C59, we conducted measurements on Wnt3-EGFP-expressing zebrafish embryos soaked in 1% DMSO, the solvent required to keep C59 in solution, and found no changes in τ_0 and D from the untreated control Wnt3-EGFP zebrafish (Figs. 3 *A* and 4 *B*; Table 1). Given residual membrane domain confinement of Wnt3-EGFP even at the highest concentration of 7.5 μM of C59 (τ_0 = 0.31 $\pm$ 0.03 s; Table 1), perhaps there are other pathways or lipid modifications not regulated by Porcupine essential for transport of Wnt3-EGFP into membrane domains. This problem could be reevaluated when alternative efficient stage-specific methods of inhibition and/or genetic ablation of Porcupine activity will be available.

Because Porcupine, a membrane-bound O-acyl transferase, is known to participate in the palmitoylation of Wnt proteins (12,19,20), our results suggest that the palmitoylation of Wnt proteins at both palmitoylation sites (cysteine and serine) is important for their intracellular trafficking into membrane domains. Our results are consistent with those of Zhai et al. (22), who demonstrated the importance of palmitoylation of Wingless, a *Drosophila* Wnt protein, by Porcupine for its eventual targeting to the cell membrane domains by the comparison of the solubility and detergent-resistant membranes-association of Wingless in whole animal lysates of wild-type and *porcupine*-deficient mutant of *Drosophila*. The membrane domain localization of palmitoylated Wnts may serve to concentrate Wnts and facilitate their extracellular trafficking by glypicans, the integral membrane proteins linked to the membrane via a glycosylphosphatidylinositol (GPI) chain found to be localized in microdomains and exposed to the extracellular matrix, which in turn

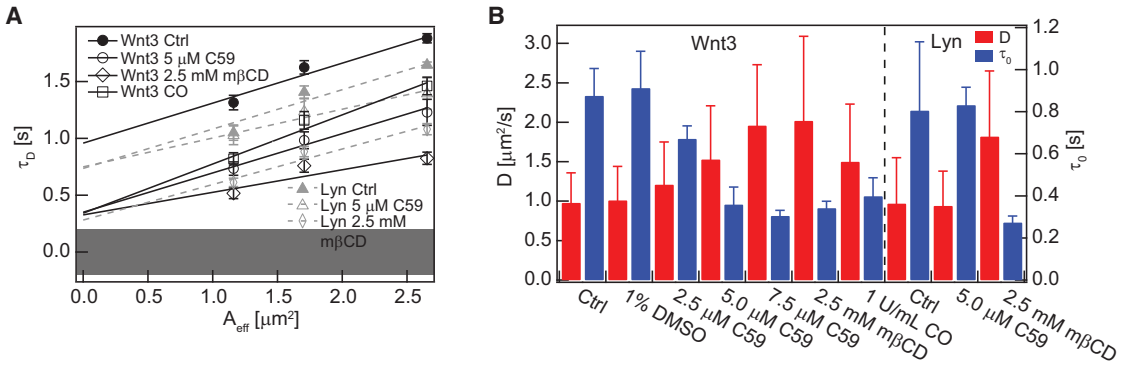

FIGURE 4 Cholesterol concentration dependence of Wnt3-EGFP and Lyn-EGFP membrane domain association in cerebellar cells of 3-dpf-old live zebrafish. (*A*) Representative SPIM-FCS diffusion law plots of Wnt3-EGFP and Lyn-EGFP after cholesterol depletion by 2.5 mM mβCD and 1 U/mL COase treatments and Porcupine inhibition by 5 μM C59 treatment. (*B*) D and τ_0 values for Wnt3-EGFP and Lyn-EGFP after various treatments. To see this figure in color, go online.

regulate Wnt signaling (65). Overall, our results show that Wnt3-EGFP is confined in membrane domains in live zebrafish embryos and this confinement is reduced upon inhibition of Porcupine by C59.

Lyn-EGFP as a negative control of palmitoylation-dependent domain confinement

We used Lyn-EGFP, a membrane tethered, raft-localized protein as a negative control to test the specificity of palmitoylation on Wnt3-EGFP domain confinement (66,67). SPIM-FCS diffusion law measurements were conducted in vivo on Lyn-EGFP. The SPIM-FCS diffusion law analysis confirmed that Lyn-EGFP is domain-confined to a similar extent as Wnt3-EGFP ($\tau_0 = 0.81 \pm 0.33$ s, Table 1). Unlike Wnt3-EGFP, 5 μM C59 treatment on Lyn-EGFP-expressing embryos did not change either τ_0 or D, which is consistent with the unchanged diffusion coefficient and membrane fraction of Lyn-EGFP previously reported by confocal FCS (25). This indicates that C59 is not influencing the membrane organization proper and that its effects are specific to Wnts, including Wnt3-EGFP (Fig. 4, *A* and *B*; Table 1).

Interestingly, upon treatment of 3-dpf-old zebrafish embryos with 2.5 mM mβCD (68), the domain confinement of both Wnt3-EGFP and Lyn-EGFP was reduced by similar extents to $\tau_0 = 0.34 \pm 0.03$ s and $\tau_0 = 0.27 \pm 0.03$ s, respectively, with a concomitant increase in diffusion coefficients by a factor of ~2 (Fig. 4 *B*; Table 1). The effects of cholesterol removal on the two proteins suggest that both proteins are similarly confined to cholesterol-dependent domains. As a further test, cholesterol was removed by COase treatment of Wnt3-EGFP-expressing zebrafish embryos. COase oxidizes cholesterol to cholestenone without any phase preference, as opposed to mβCD (51). For this purpose, 3-dpf-old zebrafish embryos were treated with 1 U/mL COase for 40 min at room temperature and measured. The effects on the domain confinement and diffusion coefficient of Wnt3-EGFP were similar for 1 U/mL COase and 2.5 mM mβCD treatment, where τ_0 decreased to 0.40 ± 0.09 s and D increased to 1.51 ± 0.71 $\mu m^2/s$ (Fig. 4, *A* and *B*; Table 1). This shows that a decrease in cholesterol levels indeed led to a redistribution of Wnt3-EGFP on the membrane with reduced domain confinement. Most likely this is due to the disruption of cholesterol-dependent domains. It is worth noting that 7.5 μM C59, 2.5 mM mβCD, and 1 U/mL COase treatments yielded comparable τ_0 and D values for Wnt3-EGFP, which further supports an idea that palmitoylated Wnt3-EGFP associates with cholesterol-dependent domains (Fig. 4 *B*).

CONCLUSIONS

In this work, we investigated the diffusion properties and membrane organization of Wnt3, a proto-oncogene signaling protein. These measurements could not be conducted in single cells as Wnt3 proteins do not properly locate to the membrane when expressed in two-dimensional cell culture (9,24). Therefore it was necessary to use SPIM-FCS in combination with the FCS diffusion law to conduct experiments in live transgenic zebrafish embryos expressing the functional Wnt3-EGFP fusion protein (25). Our results demonstrate that Wnt3-EGFP is associated with cholesterol-dependent domains in the apical membrane of cerebellar cells and its confinement is directly influenced by the activity of Porcupine, a membrane-bound O-acyltransferase, required for the palmitoylation of Wnt proteins in the ER. This membrane localization could be essential for facilitating the extracellular trafficking of Wnt3 from Wnt3-producing cells to neighboring receiving cells for proper neural patterning and development. This is, to our knowledge, the first application of SPIM-FCS to determine the membrane organization of a probe in vivo and the first demonstration that Wnt3 is associated with cholesterol-dependent lipid domains.

SUPPORTING MATERIAL

Supporting Materials and Methods, Supporting Results and Discussion, six figures, and two tables are available at http://www.biophysj.org/biophysj/supplemental/S0006-3495(16)30467-2.

AUTHOR CONTRIBUTIONS

T.W. and V.K. conceived the project; X.W.N. performed SPIM-FCS measurements and data analysis; C.T. prepared zebrafish samples; and X.W.N. and T.W. wrote the article, which was approved by all authors.

ACKNOWLEDGMENTS

The authors thank Dr. Nirmalya Bag for discussions.

X.W.N. is supported by a National University of Singapore graduate research scholarship. T.W. gratefully acknowledges funding by the Ministry of Education Singapore (grant No. MOE2014-T2-2-115). C.T. and V.K. acknowledge funding from the Agency for Science, Technology and Research of Singapore.

REFERENCES

1. Krylova, O., J. Herreros, …, P. C. Salinas. 2002. WNT-3, expressed by motoneurons, regulates terminal arborization of neurotrophin-3-responsive spinal sensory neurons. *Neuron.* 35:1043–1056.
2. Braun, M. M., A. Etheridge, …, H. Roelink. 2003. Wnt signaling is required at distinct stages of development for the induction of the posterior forebrain. *Development.* 130:5579–5587.
3. Lie, D.-C., S. A. Colamarino, …, F. H. Gage. 2005. Wnt signalling regulates adult hippocampal neurogenesis. *Nature.* 437:1370–1375.
4. Schmitt, A. M., J. Shi, …, Y. Zou. 2006. Wnt-Ryk signalling mediates medial-lateral retinotectal topographic mapping. *Nature.* 439:31–37.
5. Lewis, S. L., P.-L. Khoo, …, P. P. L. Tam. 2008. Dkk1 and Wnt3 interact to control head morphogenesis in the mouse. *Development.* 135:1791–1801.

6. Liu, P., M. Wakamiya, …, A. Bradley. 1999. Requirement for Wnt3 in vertebrate axis formation. *Nat. Genet.* 22:361–365.
7. Anne, S. L., E. E. Govek, …, M. E. Hatten. 2013. WNT3 inhibits cerebellar granule neuron progenitor proliferation and medulloblastoma formation via MAPK activation. *PLoS One.* 8:e81769.
8. Niemann, S., C. Zhao, …, U. Müller. 2004. Homozygous WNT3 mutation causes tetra-amelia in a large consanguineous family. *Am. J. Hum. Genet.* 74:558–563.
9. Coudreuse, D., and H. C. Korswagen. 2007. The making of Wnt: new insights into Wnt maturation, sorting and secretion. *Development.* 134:3–12.
10. Port, F., and K. Basler. 2010. Wnt trafficking: new insights into Wnt maturation, secretion and spreading. *Traffic.* 11:1265–1271.
11. Willert, K., J. D. Brown, …, R. Nusse. 2003. Wnt proteins are lipid-modified and can act as stem cell growth factors. *Nature.* 423:448–452.
12. Takada, R., Y. Satomi, …, S. Takada. 2006. Monounsaturated fatty acid modification of Wnt protein: its role in Wnt secretion. *Dev. Cell.* 11:791–801.
13. Herr, P., and K. Basler. 2012. Porcupine-mediated lipidation is required for Wnt recognition by Wls. *Dev. Biol.* 361:392–402.
14. Resh, M. D. 2006. Palmitoylation of ligands, receptors, and intracellular signaling molecules. *Sci. STKE.* er8:re14.
15. Levental, I., D. Lingwood, …, K. Simons. 2010. Palmitoylation regulates raft affinity for the majority of integral raft proteins. *Proc. Natl. Acad. Sci. USA.* 107:22050–22054.
16. Levental, I., M. Grzybek, and K. Simons. 2010. Greasing their way: lipid modifications determine protein association with membrane rafts. *Biochemistry.* 49:6305–6316.
17. Resh, M. D. 2013. Covalent lipid modifications of proteins. *Curr. Biol.* 23:R431–R435.
18. Kadowaki, T., E. Wilder, …, N. Perrimon. 1996. The segment polarity gene porcupine encodes a putative multitransmembrane protein involved in Wingless processing. *Genes Dev.* 10:3116–3128.
19. Tanaka, K., Y. Kitagawa, and T. Kadowaki. 2002. Drosophila segment polarity gene product porcupine stimulates the posttranslational N-glycosylation of wingless in the endoplasmic reticulum. *J. Biol. Chem.* 277:12816–12823.
20. Hofmann, K. 2000. A superfamily of membrane-bound O-acyltransferases with implications for Wnt signaling. *Trends Biochem. Sci.* 25:111–112.
21. Nusse, R. 2003. Wnts and Hedgehogs: lipid-modified proteins and similarities in signaling mechanisms at the cell surface. *Development.* 130:5297–5305.
22. Zhai, L., D. Chaturvedi, and S. Cumberledge. 2004. Drosophila Wnt-1 undergoes a hydrophobic modification and is targeted to lipid rafts, a process that requires porcupine. *J. Biol. Chem.* 279:33220–33227.
23. Lichtenberg, D., F. M. Goñi, and H. Heerklotz. 2005. Detergent-resistant membranes should not be identified with membrane rafts. *Trends Biochem. Sci.* 30:430–436.
24. Burrus, L. W., and A. P. McMahon. 1995. Biochemical analysis of murine Wnt proteins reveals both shared and distinct properties. *Exp. Cell Res.* 220:363–373.
25. Teh, C., G. Sun, …, T. Wohland. 2015. Modulating the expression level of secreted Wnt3 influences cerebellum development in zebrafish transgenics. *Development.* 142:3721–3733.
26. Wohland, T., X. Shi, …, E. H. K. Stelzer. 2010. Single plane illumination fluorescence correlation spectroscopy (SPIM-FCS) probes inhomogeneous three-dimensional environments. *Opt. Express.* 18: 10627–10641.
27. Krieger, J. W., A. P. Singh, …, T. Wohland. 2015. Imaging fluorescence (cross-) correlation spectroscopy in live cells and organisms. *Nat. Protoc.* 10:1948–1974.
28. Krieger, J. W., A. P. Singh, …, J. Langowski. 2014. Dual-color fluorescence cross-correlation spectroscopy on a single plane illumination microscope (SPIM-FCCS). *Opt. Express.* 22:2358–2375.
29. Singh, A. P., J. W. Krieger, …, T. Wohland. 2013. The performance of 2D array detectors for light sheet based fluorescence correlation spectroscopy. *Opt. Express.* 21:8652–8668.
30. Bag, N., and T. Wohland. 2014. Imaging fluorescence fluctuation spectroscopy: new tools for quantitative bioimaging. *Annu. Rev. Phys. Chem.* 65:225–248.
31. Wawrezinieck, L., H. Rigneault, …, P.-F. Lenne. 2005. Fluorescence correlation spectroscopy diffusion laws to probe the submicron cell membrane organization. *Biophys. J.* 89:4029–4042.
32. Bag, N., S. Huang, and T. Wohland. 2015. Plasma membrane organization of epidermal growth factor receptor in resting and ligand-bound states. *Biophys. J.* 109:1925–1936.
33. Huisken, J., J. Swoger, …, E. H. K. Stelzer. 2004. Optical sectioning deep inside live embryos by selective plane illumination microscopy. *Science.* 305:1007–1009.
34. Sankaran, J., N. Bag, …, T. Wohland. 2013. Accuracy and precision in camera-based fluorescence correlation spectroscopy measurements. *Anal. Chem.* 85:3948–3954.
35. Bag, N., J. Sankaran, …, T. Wohland. 2012. Calibration and limits of camera-based fluorescence correlation spectroscopy: a supported lipid bilayer study. *ChemPhysChem.* 13:2784–2794.
36. He, H.-T., and D. Marguet. 2011. Detecting nanodomains in living cell membrane by fluorescence correlation spectroscopy. *Annu. Rev. Phys. Chem.* 62:417–436.
37. Ng, X. W., N. Bag, and T. Wohland. 2015. Characterization of lipid and cell membrane organization by the fluorescence correlation spectroscopy diffusion law. *Chimia (Aarau).* 69:112–119.
38. Adler, J., A. I. Shevchuk, …, I. Parmryd. 2010. Plasma membrane topography and interpretation of single-particle tracks. *Nat. Methods.* 7:170–171.
39. Parmryd, I., and B. Önfelt. 2013. Consequences of membrane topography. *FEBS J.* 280:2775–2784.
40. Sot, J., L. A. Bagatolli, …, A. Alonso. 2006. Detergent-resistant, ceramide-enriched domains in sphingomyelin/ceramide bilayers. *Biophys. J.* 90:903–914.
41. Simons, K., and W. L. C. Vaz. 2004. Model systems, lipid rafts, and cell membranes. *Annu. Rev. Biophys. Biomol. Struct.* 33:269–295.
42. Simons, K., and D. Toomre. 2000. Lipid rafts and signal transduction. *Nat. Rev. Mol. Cell Biol.* 1:31–39.
43. Bastiani, M., and R. G. Parton. 2010. Caveolae at a glance. *J. Cell Sci.* 123:3831–3836.
44. Brown, D. A., and E. London. 1998. Functions of lipid rafts in biological membranes. *Annu. Rev. Cell Dev. Biol.* 14:111–136.
45. Parton, R. G., and A. A. Richards. 2003. Lipid rafts and caveolae as portals for endocytosis: new insights and common mechanisms. *Traffic.* 4:724–738.
46. Lingwood, D., and K. Simons. 2010. Lipid rafts as a membrane-organizing principle. *Science.* 327:46–50.
47. Simons, K., and M. J. Gerl. 2010. Revitalizing membrane rafts: new tools and insights. *Nat. Rev. Mol. Cell Biol.* 11:688–699.
48. Bag, N., D. H. X. Yap, and T. Wohland. 2014. Temperature dependence of diffusion in model and live cell membranes characterized by imaging fluorescence correlation spectroscopy. *Biochim. Biophys. Acta.* 1838:802–813.
49. Caliceti, C., L. Zambonin, …, D. Fiorentini. 2012. Effect of plasma membrane cholesterol depletion on glucose transport regulation in leukemia cells. *PLoS One.* 7:e41246.
50. Goodwin, J. S., K. R. Drake, …, A. K. Kenworthy. 2005. Ras diffusion is sensitive to plasma membrane viscosity. *Biophys. J.* 89:1398–1410.
51. Sanchez, S. A., G. Gunther, …, E. Gratton. 2011. Methyl-β-cyclodextrins preferentially remove cholesterol from the liquid disordered phase in giant unilamellar vesicles. *J. Membr. Biol.* 241:1–10.
52. Lenne, P.-F., L. Wawrezinieck, …, D. Marguet. 2006. Dynamic molecular confinement in the plasma membrane by microdomains and the cytoskeleton meshwork. *EMBO J.* 25:3245–3256.

53. Eggeling, C., C. Ringemann, …, S. W. Hell. 2009. Direct observation of the nanoscale dynamics of membrane lipids in a living cell. *Nature.* 457:1159–1162.

54. Masuda, A., K. Ushida, and T. Okamoto. 2005. New fluorescence correlation spectroscopy enabling direct observation of spatiotemporal dependence of diffusion constants as an evidence of anomalous transport in extracellular matrices. *Biophys. J.* 88:3584–3591.

55. He, J., S.-M. Guo, and M. Bathe. 2012. Bayesian approach to the analysis of fluorescence correlation spectroscopy data I: theory. *Anal. Chem.* 84:3871–3879.

56. Guo, S.-M., J. He, …, M. Bathe. 2012. Bayesian approach to the analysis of fluorescence correlation spectroscopy data II: application to simulated and in vitro data. *Anal. Chem.* 84:3880–3888.

57. Sun, G., S.-M. Guo, …, T. Wohland. 2015. Bayesian model selection applied to the analysis of fluorescence correlation spectroscopy data of fluorescent proteins in vitro and in vivo. *Anal. Chem.* 87:4326–4333.

58. Guo, S.-M., N. Bag, …, M. Bathe. 2014. Bayesian total internal reflection fluorescence correlation spectroscopy reveals hIAPP-induced plasma membrane domain organization in live cells. *Biophys. J.* 106:190–200.

59. van den Heuvel, M., C. Harryman-Samos, …, R. Nusse. 1993. Mutations in the segment polarity genes wingless and porcupine impair secretion of the Wingless protein. *EMBO J.* 12:5293–5302.

60. Biechele, S., B. J. Cox, and J. Rossant. 2011. Porcupine homolog is required for canonical Wnt signaling and gastrulation in mouse embryos. *Dev. Biol.* 355:275–285.

61. Proffitt, K. D., and D. M. Virshup. 2012. Precise regulation of porcupine activity is required for physiological Wnt signaling. *J. Biol. Chem.* 287:34167–34178.

62. Coombs, G. S., J. Yu, …, D. M. Virshup. 2010. WLS-dependent secretion of WNT3A requires Ser^{209} acylation and vacuolar acidification. *J. Cell Sci.* 123:3357–3367.

63. Galli, L. M., and L. W. Burrus. 2011. Differential palmit(e)oylation of Wnt1 on C93 and S224 residues has overlapping and distinct consequences. *PLoS One.* 6:e26636.

64. Gao, X., and R. N. Hannoush. 2014. Single-cell imaging of Wnt palmitoylation by the acyltransferase porcupine. *Nat. Chem. Biol.* 10:61–68.

65. Sakane, H., H. Yamamoto, …, A. Kikuchi. 2012. Localization of glypican-4 in different membrane microdomains is involved in the regulation of Wnt signaling. *J. Cell Sci.* 125:449–460.

66. Kovárová, M., P. Tolar, …, P. Dráber. 2001. Structure-function analysis of Lyn kinase association with lipid rafts and initiation of early signaling events after Fcε receptor I aggregation. *Mol. Cell. Biol.* 21:8318–8328.

67. Ingley, E. 2012. Functions of the Lyn tyrosine kinase in health and disease. *Cell Commun. Signal.* 10:21.

68. Abu-Siniyeh, A., D. M. Owen, …, K. Gaus. 2016. The aPKC/Par3/Par6 polarity complex and membrane order are functionally interdependent in epithelia during vertebrate organogenesis. *Traffic.* 17:66–79.